

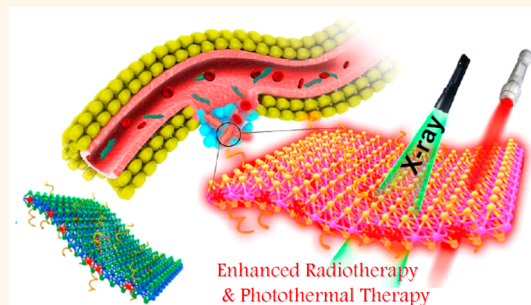
# Bottom-Up Synthesis of Metal-Ion-Doped WS<sub>2</sub> Nanoflakes for Cancer Theranostics

Liang Cheng,<sup>\*,†,§</sup> Chao Yuan,<sup>†,§</sup> Sida Shen,<sup>†</sup> Xuan Yi,<sup>‡</sup> Hua Gong,<sup>†</sup> Kai Yang,<sup>‡</sup> and Zhuang Liu<sup>\*,†</sup>

<sup>†</sup>Institute of Functional Nano & Soft Materials (FUNSOM), Collaborative Innovation Center of Suzhou Nano Science and Technology, Soochow University, Suzhou, Jiangsu 215123, China and <sup>‡</sup>School of Radiation Medicine and Protection & School for Radiological and Interdisciplinary Sciences (RAD-X), Jiangsu Provincial Key Laboratory of Radiation Medicine and Protection, Soochow University, Suzhou, Jiangsu 215123, China. <sup>§</sup>L. Cheng and C. Yuan contributed equally to this work.

**ABSTRACT** Recently, two-dimensional transition metal dichalcogenides (TMDCs) have received tremendous attention in many fields including biomedicine. Herein, we develop a general method to dope different types of metal ions into WS<sub>2</sub> nanoflakes, a typical class of TMDCs, and choose Gd<sup>3+</sup>-doped WS<sub>2</sub> (WS<sub>2</sub>:Gd<sup>3+</sup>) with polyethylene glycol (PEG) modification as a multifunctional agent for imaging-guided combination cancer treatment. While WS<sub>2</sub> with strong near-infrared (NIR) absorbance and X-ray attenuation ability enables contrasts in photoacoustic (PA) imaging and computed tomography (CT), Gd<sup>3+</sup> doping offers the nanostructure a paramagnetic property for magnetic resonance (MR) imaging.

As revealed by trimodal PA/CT/MR imaging, WS<sub>2</sub>:Gd<sup>3+</sup>-PEG nanoflakes showed efficient tumor homing after intravenous injection. *In vivo* cancer treatment study further uncovered that WS<sub>2</sub>:Gd<sup>3+</sup>-PEG could not only convert NIR light into heat for photothermal therapy (PTT) but also enhance the ionizing irradiation-induced tumor damage to boost radiation therapy (RT). Owing to the improved tumor oxygenation after the mild PTT, the combination of PTT and RT induced by WS<sub>2</sub>:Gd<sup>3+</sup>-PEG resulted in a remarkable synergistic effect to destroy cancer. Our work highlights the promise of utilizing inherent physical properties of TMDC-based nanostructures, whose functions could be further enriched by elementary doping, for applications in multimodal bioimaging and synergistic cancer therapy.



**KEYWORDS:** metal-ion-doped WS<sub>2</sub> nanoflakes · cancer theranostics · multimodal imaging · radiation therapy · photothermal therapy

Since cancer has become one of the greatest threats to human health, many new therapeutic strategies have been explored in recent years.<sup>1,2</sup> In particular, nanomedicine, with many interesting nanomaterials or nanotechnologies involved to either improve the therapeutic outcomes of currently used cancer therapies or to kill cancer by nonconventional methods, has shown great promise in recent years. For example, numerous types of nanocarriers have been developed to realize tumor-targeted drug delivery, aiming at improving therapeutic efficacy and/or reducing side effects of chemotherapy.<sup>3</sup> To enhance the efficiency of radiation therapy (RT), nanoparticles containing high-Z elements (e.g., Au, I, Bi, and rare earth elements), which are able to interact with and absorb ionizing radiation, have been explored in order to concentrate the radiation dose in the tumor.<sup>4–9</sup> Moreover, as a minimally invasive

therapy approach, near-infrared (NIR) laser-induced-photothermal therapy (PTT) utilizing heating of NIR-absorbing nanoagents in the tumor to destroy cancer has also received wide interest in recent years.<sup>10–17</sup> On the other hand, to optimize the treatment planning and monitor the therapeutic responses, imaging-guided therapy has been proposed as an encouraging strategy to realize personalized medicine.<sup>18–20</sup> To achieve the above aims, theranostic nanostructures that have highly integrated noncompromised functions and can be fabricated by relatively simple/reliable methods would be of great interest.

Recently, transition metal dichalcogenides (TMDCs) such as MoS<sub>2</sub>, MoSe<sub>2</sub>, WS<sub>2</sub>, and WSe<sub>2</sub>, which consist of hexagonal layers of metal atoms (M) sandwiched between two layers of chalcogen atoms (X) with stoichiometry MX<sub>2</sub>, have been widely explored in many different fields.<sup>21–28</sup> Lately a number

\* Address correspondence to  
zliu@suda.edu.cn,  
lcheng2@suda.edu.cn.

Received for review July 24, 2015  
and accepted October 7, 2015.

Published online October 07, 2015  
10.1021/acsnano.5b04606

© 2015 American Chemical Society

of groups including ours have found that TMDC nanosheets are also promising for applications in biomedicine.<sup>28–31</sup> Due to their high absorbance in the NIR region, we and others have used MoS<sub>2</sub>, WS<sub>2</sub>, TiS<sub>2</sub>, or Bi<sub>2</sub>Se<sub>3</sub> nanosheets as photothermal agents for cancer treatment.<sup>28,30,32–34</sup> Utilizing the rather large surface area of these atomic-thin nanosheets, TMDCs have also been explored as drug delivery platforms for combination therapy of cancer.<sup>31,35</sup> Moreover, certain types of TMDCs, such as WS<sub>2</sub> and Bi<sub>2</sub>Se<sub>3</sub>, which contain high-Z elements, could serve as contrast agents in X-ray computed tomography (CT) imaging.<sup>30,33,34,36</sup> By attaching magnetic nanoparticles or absorbing with radioactive isotopes, multimodal magnetic resonance (MR)/nuclear imaging with TMDCs has further been demonstrated in recent studies.<sup>37,38</sup> TMDCs have thus appeared to be an interesting class of nanomaterials that are promising in cancer theranostics.

However, many of TMDC-based nanoagents previously used in biomedicine are prepared by exfoliation of their bulk counterparts and have fixed elemental compositions. Recently, we have developed a bottom-up method to prepare high-quality WS<sub>2</sub> nanoflakes as catalysts for the high-performance hydrogen evolution reaction.<sup>39,40</sup> Therefore, we wonder if we can use this method to fabricate new generations of TMDC agents with further enriched functions *via* doping with other elements of interest. Herein, for the first time, we developed a bottom-up solution-phase method to synthesize WS<sub>2</sub> nanoflakes intrinsically doped with different types of metal ions (*e.g.*, Fe<sup>3+</sup>, Co<sup>2+</sup>, Ni<sup>2+</sup>, Mn<sup>2+</sup>, Gd<sup>3+</sup>) and chose Gd<sup>3+</sup>-doped WS<sub>2</sub> (WS<sub>2</sub>:Gd<sup>3+</sup>) nanoflakes as a typical example to realize combined photothermal and radiation therapy under the guidance of trimodal imaging. After poly(ethylene glycol) (PEG) modification, the obtained PEGylated WS<sub>2</sub>:Gd<sup>3+</sup> nanoflakes were stable in physiological solutions. Utilizing the strong NIR absorbance of WS<sub>2</sub>, the paramagnetic property contributed from the doped Gd<sup>3+</sup>, and X-ray attenuation ability of this nanostructure, *in vivo* photoacoustic (PA), MR, and CT trimodal imaging was realized, revealing efficient passive tumor targeting of those nanoflakes after intravenous (i.v.) injection. We further utilized WS<sub>2</sub>:Gd<sup>3+</sup>-PEG nanoflakes to enable PTT and enhance RT, whose combination resulted in highly effective synergistic tumor destruction after i.v. injection of WS<sub>2</sub>:Gd<sup>3+</sup>-PEG followed by NIR laser + X-ray irradiation of tumors, without showing obvious toxicity to the treated animals. Our work presents a simple method to fabricate metal-ion-doped TMDC nanostructures with highly enriched properties and functions, which are promising for a wide range of applications including cancer theranostics.

## RESULTS AND DISCUSSION

The fabrication of metal-ion doped WS<sub>2</sub> nanoflakes and the subsequent functionalization with PEG is illustrated

in Figure 1A. We prepared WS<sub>2</sub>:M<sup>n+</sup> (M = Fe<sup>3+</sup>, Co<sup>3+</sup>, Ni<sup>2+</sup>, Mn<sup>2+</sup>, and Gd<sup>3+</sup>) with different metal doping levels in WS<sub>2</sub> nanoflakes using a high-temperature solution method by reacting WCl<sub>6</sub> and MCl<sub>x</sub> (M = Fe<sup>3+</sup>, Co<sup>3+</sup>, Ni<sup>2+</sup>, Mn<sup>2+</sup>, and Gd<sup>3+</sup>) with sulfur dissolved in a mixed solvent of oleylamine (OM) and 1-octadecene (ODE) at 300 °C under a N<sub>2</sub> atmosphere. During the course of the reaction, the tungsten and other metal precursors would first form complexes with OM. Upon injection of the sulfur solution, the solution color immediately turned to black, suggesting rapid formation of WS<sub>2</sub>:M<sup>n+</sup> (M = Fe<sup>3+</sup>, Co<sup>3+</sup>, Ni<sup>2+</sup>, Mn<sup>2+</sup>, and Gd<sup>3+</sup>) nanoflakes. Excess OM and ODE were removed by centrifugation. The exact W:M molar ratios in the obtained WS<sub>2</sub>:M<sup>n+</sup> (M = Fe<sup>3+</sup>, Co<sup>3+</sup>, Ni<sup>2+</sup>, Mn<sup>2+</sup>, and Gd<sup>3+</sup>) samples were measured by inductively coupled plasma atomic emission spectroscopy (ICP-AES). As shown in Figure 1B–F, the metal-ion doping ratios in the final products increased with the rise of added doping metal ions during reaction. For example, the exact W:Gd ratio in the WS<sub>2</sub>:Gd<sup>3+</sup> nanoflakes was 94.6:5.4 (WS<sub>2</sub>:Gd<sup>3+</sup>-1), 86.7:13.3 (WS<sub>2</sub>:Gd<sup>3+</sup>-2), and 84.3:15.7 (WS<sub>2</sub>:Gd<sup>3+</sup>-3) for samples prepared with W:Gd feeding ratios of 90:10, 80:20, and 70:30, respectively.

Transmission electron microscopy (TEM) images of as-synthesized WS<sub>2</sub>:M<sup>n+</sup> (M = Fe<sup>3+</sup>, Co<sup>3+</sup>, Ni<sup>2+</sup>, Mn<sup>2+</sup>, and Gd<sup>3+</sup>) with different ratios of metal-ion doping all showed flake-like morphology with the dark-contrast lines representing their standing edges (Figure 2, left row). The interplanar size of WS<sub>2</sub>:Gd<sup>3+</sup>-3 was measured to be ~0.268 nm (Supporting Figure S1), a value consistent with the spacing of the WS<sub>2</sub> (100) plane. To further confirm the compositions and illustrate the structures of the synthesized hybrid materials (WS<sub>2</sub>:Fe<sup>3+</sup>, WS<sub>2</sub>:Co<sup>2+</sup>, WS<sub>2</sub>:Ni<sup>2+</sup>, WS<sub>2</sub>:Mn<sup>2+</sup>, and WS<sub>2</sub>:Gd<sup>3+</sup>), scanning transmission electron microscopy with energy-dispersive X-ray spectroscopy (STEM-EDS) mapping of elements (Figure 2, right row) showed that the distributions of W, S, and other M elements (Fe<sup>3+</sup>, Co<sup>2+</sup>, Ni<sup>2+</sup>, Mn<sup>2+</sup>, and Gd<sup>3+</sup>) were largely colocalized for WS<sub>2</sub>:Fe<sup>3+</sup>-3, WS<sub>2</sub>:Co<sup>2+</sup>-3, WS<sub>2</sub>:Ni<sup>2+</sup>-3, WS<sub>2</sub>:Mn<sup>2+</sup>-3, and WS<sub>2</sub>:Gd<sup>3+</sup>-3 samples, suggesting that various types of metal ions were homogeneously doped inside the as-prepared WS<sub>2</sub>:M<sup>n+</sup> (Fe<sup>3+</sup>, Co<sup>3+</sup>, Ni<sup>2+</sup>, Mn<sup>2+</sup>, and Gd<sup>3+</sup>) nanoflakes. We have thus successfully developed a simple bottom-up solution-phase method that is generally applicable to synthesize various types of metal-ion-doped WS<sub>2</sub> nanoflakes.

Gd<sup>3+</sup>-containing nanostructures have been extensively used as an effective contrast agent in T1-weighted MR imaging. We then chose Gd<sup>3+</sup>-doped WS<sub>2</sub> nanoflakes as an example for the subsequent research. The structure information on the obtained WS<sub>2</sub>:Gd<sup>3+</sup> nanoflakes was further analyzed by X-ray diffractometer (XRD). As shown in Supporting Figure S2, the representative diffraction peaks in the XRD spectrum of WS<sub>2</sub>

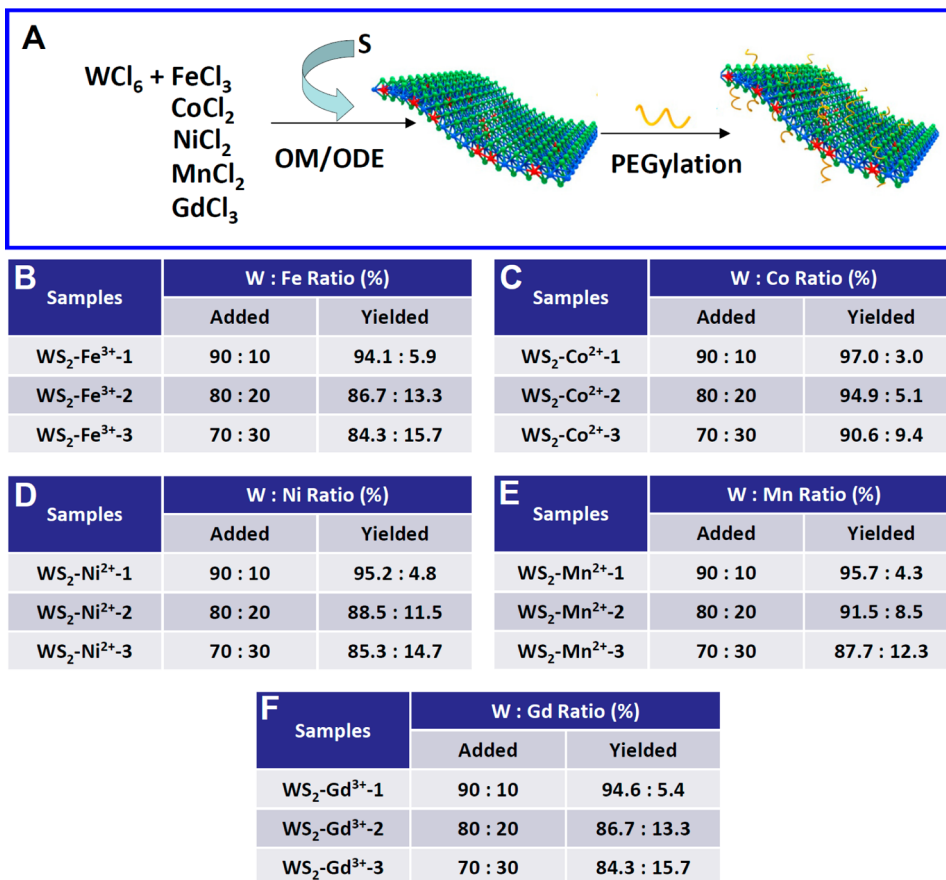


**Figure 1.** Synthesis and composition analysis of WS<sub>2</sub>:M<sup>n+</sup> (M = Fe<sup>3+</sup>, Co<sup>2+</sup>, Ni<sup>2+</sup>, Mn<sup>2+</sup>, and Gd<sup>3+</sup>) nanoflakes prepared by a bottom-up method. (A) Scheme showing the one-pot synthesis of metal-ion-doped WS<sub>2</sub> nanoflakes and the subsequent surface modification with PEG. (B–F) Tables showing element compositions of the various metal-ion-doped WS<sub>2</sub> nanoflakes as determined by ICP-AES: (B) WS<sub>2</sub>:Fe<sup>3+</sup> nanoflakes; (C) WS<sub>2</sub>:Co<sup>2+</sup> nanoflakes; (D) WS<sub>2</sub>:Ni<sup>2+</sup> nanoflakes; (E) WS<sub>2</sub>:Mn<sup>2+</sup> nanoflakes; and (F) WS<sub>2</sub>:Gd<sup>3+</sup> nanoflakes.

nanoflakes matched well with the standard pattern of WS<sub>2</sub> (JCPDS card, No. 084-1398). Those peaks showed no significant change after Gd<sup>3+</sup>-doping, indicating that introducing Gd<sup>3+</sup> would not affect the crystalline structure of WS<sub>2</sub>. To further evaluate the nanoflakes' composition and oxidation state, X-ray photoelectron spectroscopy (XPS) characterization was performed. Two peaks centered at 31.99 and 34.19 eV (Supporting Figure S3), which corresponded to W 4f<sub>7/2</sub> and W 4f<sub>5/2</sub> peaks of W<sup>4+</sup> ions, respectively, were observed in the XPS spectrum of WS<sub>2</sub>:Gd<sup>3+</sup>-3. The peak located at 143.9 eV could be assigned to Gd 3d<sub>5/2</sub>, while those located at 161.7 and 162.8 eV were assigned to S 2p<sub>3/2</sub> and S 2p<sub>1/2</sub>, respectively. No peaks were detected for metallic W, Gd, and other impurities, indicating the high purity of the as-prepared Gd<sup>3+</sup>-doped WS<sub>2</sub> nanoflakes.

For biomedical applications, the synthesized hydrophobic WS<sub>2</sub>:Gd<sup>3+</sup> nanoflakes have to be transferred into the aqueous phase. An amphiphilic polymer, poly(ethylene glycol)-grafted poly(maleic anhydride-*alt*-1-octadecene) (C<sub>18</sub>PMH-PEG), was used to modify WS<sub>2</sub>:Gd<sup>3+</sup> nanoflakes. It was found that the average size of the PEGylated WS<sub>2</sub>:Gd<sup>3+</sup> nanoflakes decreased to ~80 nm (Figure 3A), probably due to the ultrasonication

during the PEG coating step. The hydrodynamic size of the WS<sub>2</sub>:Gd<sup>3+</sup> nanoflakes in water was measured by dynamic light scattering (DLS) to be 90–100 nm (Figure 3B). Fourier-transform infrared spectroscopy (FTIR) and thermogravimetric analysis (TG) (Supporting Figure S4A,B) curves of the WS<sub>2</sub>:Gd<sup>3+</sup>-3-PEG nanoflakes all evidenced the successful surface grafting of PEG. After surface modification, the obtained WS<sub>2</sub>:Gd<sup>3+</sup>-PEG nanoflakes with different Gd<sup>3+</sup>-doping ratios exhibited excellent stability in various physiological solutions, including saline, cell medium, and serum (Supporting Figure S5). Importantly, the Gd<sup>3+</sup> doping in WS<sub>2</sub> nanoflakes appeared to be very stable without being leaked from those nanoflakes (Supporting Figure S6), whereas free Gd<sup>3+</sup> showed no appreciable adsorption on the surface of WS<sub>2</sub> upon mixing in the aqueous solution (data not shown), both indicating that Gd<sup>3+</sup> was doped inside WS<sub>2</sub> instead of simple physical adsorption.

Next, we carefully studied the physical properties of our WS<sub>2</sub>:Gd<sup>3+</sup>-PEG nanoflakes. UV-vis-NIR spectra of WS<sub>2</sub>:Gd<sup>3+</sup>-PEG nanoflakes with different ratios of Gd<sup>3+</sup> doping (Figure 3C) showed similarly high absorbance in a wide spectral range of 700–1000 nm. The mass

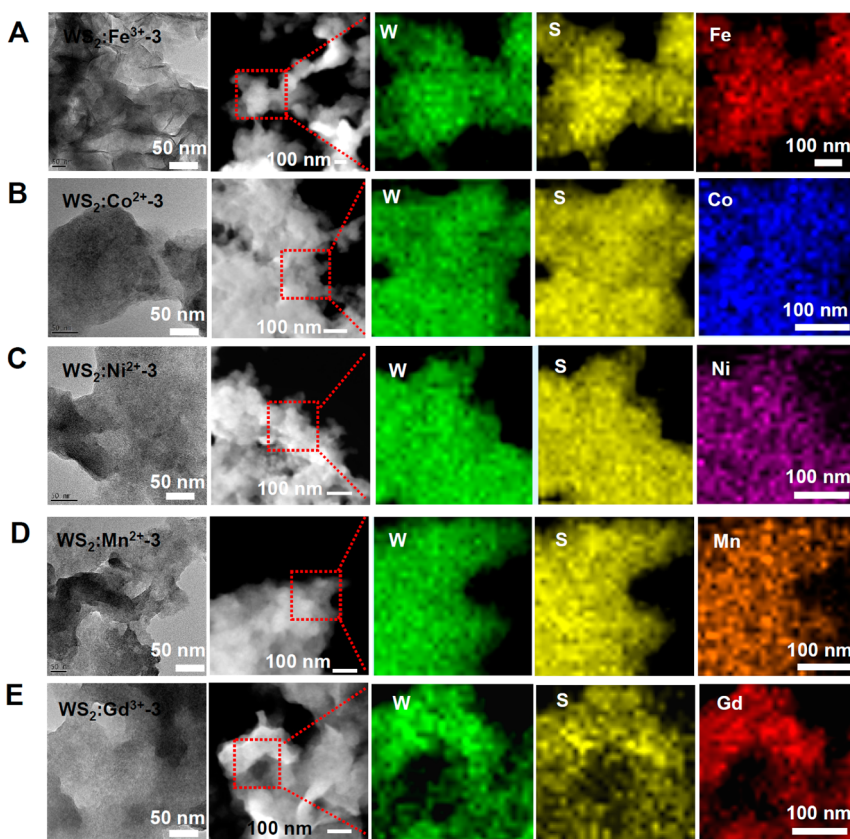


**Figure 2.** TEM and STEM-EDS mapping of metal-ion-doped  $\text{WS}_2$  nanoflakes: (A)  $\text{WS}_2:\text{Fe}^{3+}$  nanoflakes; (B)  $\text{WS}_2:\text{Co}^{2+}$  nanoflakes; (C)  $\text{WS}_2:\text{Ni}^{2+}$  nanoflakes; (D)  $\text{WS}_2:\text{Mn}^{2+}$  nanoflakes; and (E)  $\text{WS}_2:\text{Gd}^{3+}$  nanoflakes. The excellent colocalization of three different elements in these samples suggested that metal ions were evenly doped inside the  $\text{WS}_2$  nanoflakes.

extinction coefficient of  $\text{WS}_2:\text{Gd}^{3+}$ -PEG was measured to be  $22.6 \text{ L g}^{-1} \text{ cm}^{-1}$ , which was a little lower than that of  $\text{WS}_2$  nanosheets ( $23.8 \text{ L g}^{-1} \text{ cm}^{-1}$ ) synthesized by exfoliation, but much higher than that of graphene oxide (GO,  $3.6 \text{ L g}^{-1} \text{ cm}^{-1}$ ).<sup>30</sup> After the NIR laser irradiation, all three types of  $\text{WS}_2:\text{Gd}^{3+}$ -PEG nanoflakes with different  $\text{Gd}^{3+}$ -doping ratios showed obvious concentration-dependent temperature increases, as well as great photostability under laser irradiation (Figure 3D, Supporting Figure S7), allowing them to be used as effective photothermal agents.

X-ray computed tomography imaging is one of the most commonly used imaging tools for clinic diagnosis and medical research due to its deep tissue penetration and high-resolution characteristics.<sup>41</sup> Many high atomic number elements such as Au, Bi, Y, Mo, and W have been reported for contrast enhancement in CT imaging.<sup>30,41–43</sup> Herein, we also investigated the use of PEGylated  $\text{WS}_2:\text{Gd}^{3+}$  nanoflakes as CT contrast agents. Figure 3E,F present CT images and Hounsfield units (HU) values of three types of  $\text{WS}_2:\text{Gd}^{3+}$ -PEG nanoflakes with different concentrations in water. As expected, the CT contrast of those samples showed sharp signal enhancement as the  $\text{WS}_2:\text{Gd}^{3+}$ -PEG concentrations increase. The slopes of the concentration-dependent HU values for  $\text{WS}_2:\text{Gd}^{3+}$ -1-PEG,  $\text{WS}_2:\text{Gd}^{3+}$ -2-PEG, and  $\text{WS}_2:\text{Gd}^{3+}$ -3-PEG were determined to be 25.9, 23.7, and

19.9 HU L/g, respectively, which appeared to be higher than that of iopromide (14.76 HU L/g), a commercial iodine-based CT contrast agent used in the clinic.<sup>44</sup> These results demonstrated that  $\text{WS}_2:\text{Gd}^{3+}$ -PEG nanoflakes may be a promising contrast agent for CT imaging.

Agents containing paramagnetic  $\text{Gd}^{3+}$  have been widely used in the clinic to enhance the T1 contrast in MR imaging. To explore the possibility of using our synthesized  $\text{WS}_2:\text{Gd}^{3+}$ -PEG nanoflakes as a T1-weighted MR contrast agent, we measured their T1 relaxation time under different concentrations (Figure 3G,H). An obvious concentration-dependent brightening effect in T1-weighted MR images was seen for all three types of  $\text{Gd}^{3+}$ -doped  $\text{WS}_2$  nanoflakes with PEGylation (Figure 3G). The T1 relaxivities ( $r_1$ ) of the  $\text{WS}_2:\text{Gd}^{3+}$ -1-PEG,  $\text{WS}_2:\text{Gd}^{3+}$ -2-PEG, and  $\text{WS}_2:\text{Gd}^{3+}$ -3-PEG were measured to be  $16.7$ ,  $10.40$ , and  $7.03 \text{ mM}^{-1} \text{ s}^{-1}$ , respectively, which were much higher than that of the clinic-approved T1MR contrast agent Magnevist ( $4.29 \text{ mM}^{-1} \text{ s}^{-1}$ ), probably due to the increased local concentration of  $\text{Gd}^{3+}$  and lowered molecular tumbling rate in those nanostructures, similar to those observed in other  $\text{Gd}^{3+}$ -containing complexes reported previously.<sup>45–48</sup> With the increase of  $\text{Gd}^{3+}$ -doping ratios, the T1 relaxivity was greatly enhanced. Considering the fact that  $\text{WS}_2:\text{Gd}^{3+}$ -3-PEG offered

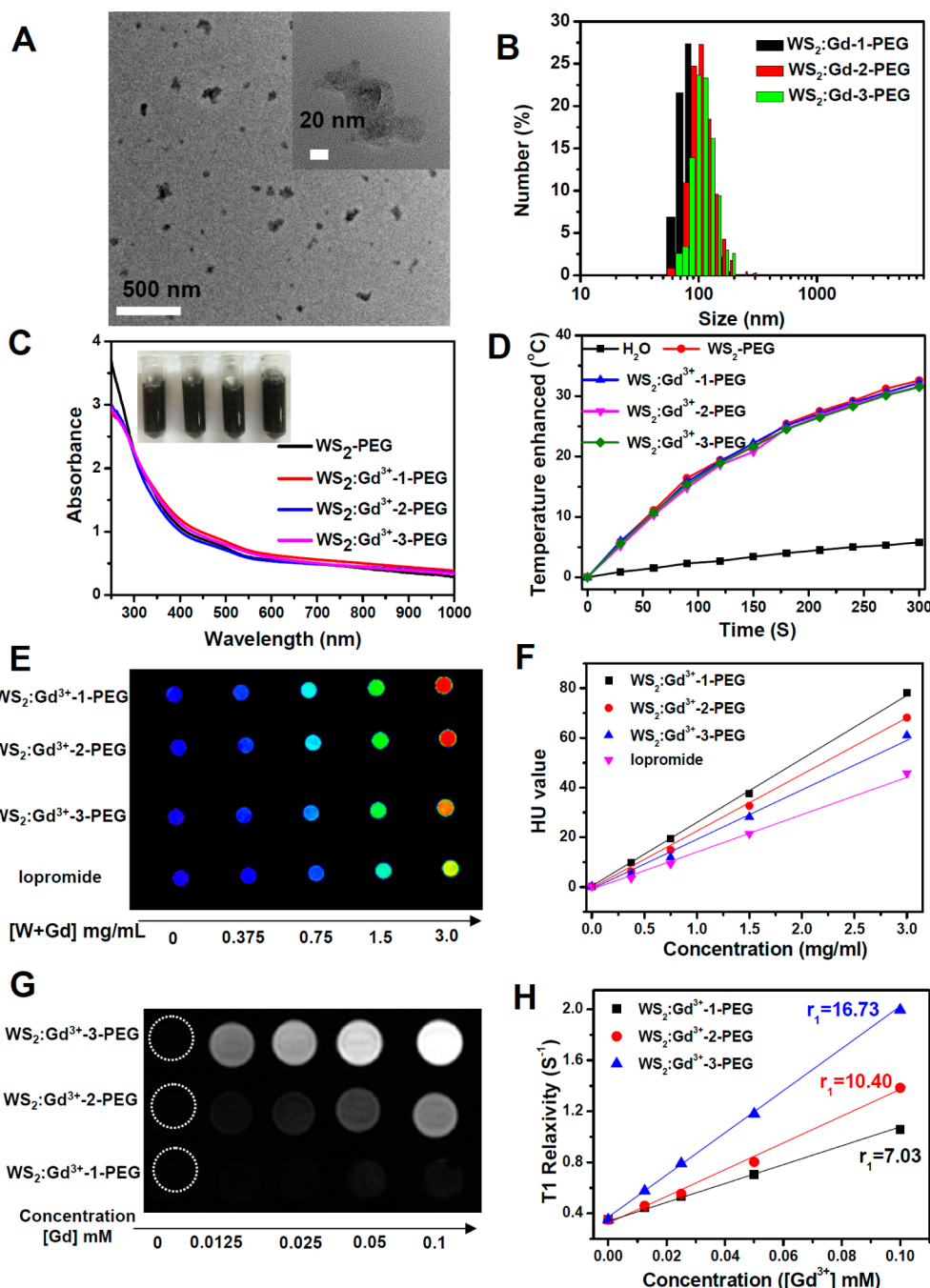


**Figure 3. Characterization of PEGylated WS<sub>2</sub>:Gd<sup>3+</sup> nanoflakes.** (A) TEM image of WS<sub>2</sub>:Gd<sup>3+</sup>-3-PEG nanoflakes. Inset is a magnified TEM image. (B) DLS-measured diameters of the three types of PEGylated WS<sub>2</sub>:Gd<sup>3+</sup> nanoflakes in water. (C) UV-vis-NIR absorbance spectra of WS<sub>2</sub> and WS<sub>2</sub>:Gd<sup>3+</sup> nanoflakes with different Gd-doping ratios. Inset: Photograph of the respective solutions in water. (D) Photothermal heating curves of WS<sub>2</sub>-PEG and WS<sub>2</sub>:Gd<sup>3+</sup>-PEG solutions with concentrations of 0.5 mg/mL under 808 nm laser irradiation at a power density of 0.8 W/cm<sup>2</sup>. (E, F) CT images (E) and HU values (F) of WS<sub>2</sub>:Gd<sup>3+</sup>-PEG solutions with different concentrations. (G, H) T1-weighted MR images (G) and T1 relaxation rate (H) of WS<sub>2</sub>:Gd<sup>3+</sup>-PEG solutions with different concentrations.

much stronger T1 contrast in MR imaging and only slightly lower NIR and X-ray absorbance ability compared to the other two types of Gd<sup>3+</sup>-doped WS<sub>2</sub> with lower doping ratios, we chose WS<sub>2</sub>:Gd<sup>3+</sup>-3-PEG nanoflakes for the next *in vitro* and *in vivo* experiments.

Motivated by the excellent photothermal property of WS<sub>2</sub>:Gd<sup>3+</sup>-PEG nanoflakes, we continued to test the efficacy of WS<sub>2</sub>:Gd<sup>3+</sup>-PEG nanoflakes for *in vitro*

photothermal cancer therapy. The standard methyl thiazolyl tetrazolium (MTT) assay was first carried out to determine the relative viabilities of 4T1 murine breast cancer cells. After cells were incubated with WS<sub>2</sub>:Gd<sup>3+</sup>-PEG nanoflakes at various concentrations for 24 and 48 h (Supporting Figure S8), no significant cytotoxicity of these WS<sub>2</sub> nanoflakes was observed even at high concentrations up to 0.1 mg/mL. Next, we used

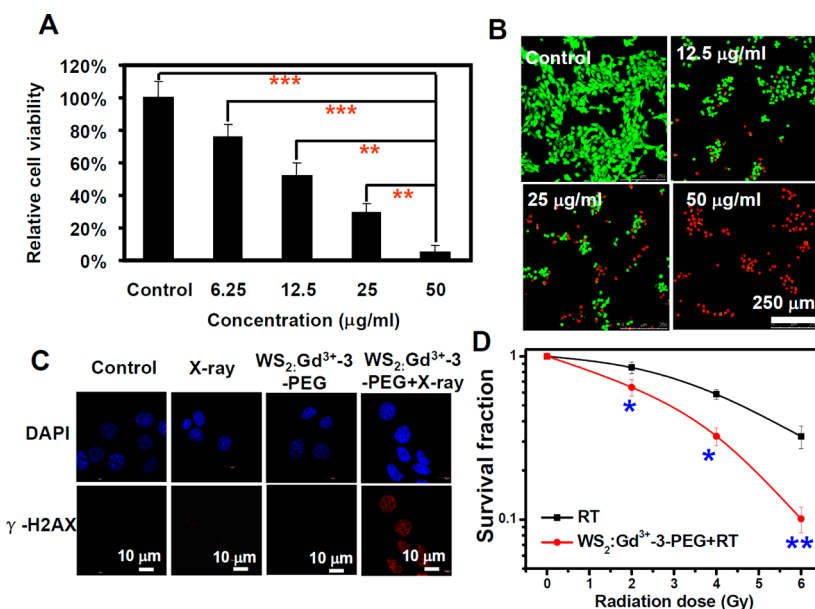


**Figure 4.** *In vitro* photothermal therapy and radiation therapy. (A) Relative viabilities of 4T1 cells after  $\text{WS}_2:\text{Gd}^{3+}$ -3-PEG-induced photothermal ablation at different concentrations of nanoflakes. Error bars were based on the standard deviations (SD) of six parallel samples.  $p$  values were calculated by the methodology of Tukey's post-test (\*\* $p < 0.001$ , \*\* $p < 0.01$ , or \* $p < 0.05$ ). (B) Confocal images of calcine AM (green, live cells) and propidium iodide (red, dead cells) costained cells after incubation with different concentration of  $\text{WS}_2:\text{Gd}^{3+}$ -3-PEG and being exposed to the 808 nm laser at a power density of  $0.8 \text{ W/cm}^2$  for 5 min. (C) Confocal fluorescence images of  $\gamma$ -H2AX-stained 4T1 cells treated with PBS control, RT alone (4 Gy),  $\text{WS}_2:\text{Gd}^{3+}$ -3-PEG control, and  $\text{WS}_2:\text{Gd}^{3+}$ -3-PEG + RT (4 Gy). (D) Clonogenic survival assay of 4T1 cells treated with or without  $\text{WS}_2:\text{Gd}^{3+}$ -3-PEG under a series of radiation doses of 0, 2, 4, and 6 Gy. Error bars represent SD of at least three replicates.  $p$  values: \* $p < 0.05$ , \*\* $p < 0.01$ .

$\text{WS}_2:\text{Gd}^{3+}$ -PEG nanoflakes as a photothermal agent for *in vitro* cancer cell ablation under laser irradiation. 4T1 cells were incubated with different concentrations of  $\text{WS}_2:\text{Gd}^{3+}$ -PEG nanoflakes for 12 h and then irradiated by the 808 nm laser for 5 min at a power density of  $0.8 \text{ W/cm}^2$ . Cell viability assay was conducted to determine the cancer cell killing efficiencies of PTT at different concentrations of  $\text{WS}_2:\text{Gd}^{3+}$ -PEG (Figure 4A). As expected, enhanced cancer cell ablation was observed as the nanoflake concentrations increased. Confocal fluorescence images of calcine AM and propidium iodide (PI) costained cells further confirmed the effective and specific photothermal ablation of 4T1 cells induced by  $\text{WS}_2:\text{Gd}^{3+}$ -PEG nanoflakes. In contrast, cells without  $\text{WS}_2:\text{Gd}^{3+}$ -PEG nanoflake incubation were not affected after laser irradiation (Figure 4B).

To test the potential radio-sensitization capability,  $\text{WS}_2:\text{Gd}^{3+}$ -PEG-enhanced X-ray radiation therapy of 4T1 cells was evaluated by  $\gamma$ -H2AX immunofluorescence to investigate the RT-induced DNA damage to cells<sup>49</sup> and the clonogenic survival assay to evaluate the *in vitro* efficacy of radiotherapy. As shown in Figure 4C, immunofluorescent images revealed very low levels of  $\gamma$ -H2AX fluorescent spots in PBS-treated cells regardless of X-ray irradiation, as well as cells incubated with  $\text{WS}_2:\text{Gd}^{3+}$ -PEG in the absence of X-ray irradiation. In contrast, high levels of  $\gamma$ -H2AX foci, an indicator of double-strand DNA breaking, were observed within nuclei of cells incubated with

$\text{WS}_2:\text{Gd}^{3+}$ -PEG after X-ray irradiation (dose = 4 Gy). The clonogenic survival assay further revealed that incubation of cancer cells with  $\text{WS}_2:\text{Gd}^{3+}$ -PEG could remarkably enhance the RT efficacy, which showed an obvious irradiation-dose-dependent nature (Figure 4D, Supporting Figure S9). The ability of  $\text{WS}_2:\text{Gd}^{3+}$ -PEG to enhance the efficacy of RT could possibly be attributed to the strong X-ray attenuation ability of W and Gd elements, so as to concentrate the irradiation energy of X-ray and generate secondary and Auger electrons within cancer cells, thus resulting in DNA damage and cell growth inhibition.<sup>6</sup>

Utilizing the interesting optical, magnetic, and X-ray absorbance properties of Gd<sup>3+</sup>-doped  $\text{WS}_2:\text{Gd}^{3+}$  nanoflakes, we next conducted triple-modal CT/MR/PA imaging for tumor-bearing mice post intravenous injection of  $\text{WS}_2:\text{Gd}^{3+}$ -PEG. In our experiments, Balb/c mice bearing 4T1 tumors were i.v. injected with  $\text{WS}_2:\text{Gd}^{3+}$ -PEG nanoflakes ( $5 \text{ mg/mL}, 200 \mu\text{L}$ ) and then imaged at 24 h postinjection (p.i.) by a GE Discovery CT750HD CT instrument (Figure 5A). Strong tumor contrast was observed in the CT image, with the tumor HU value dramatically increased from  $33.6 \pm 2.5 \text{ HU}$  before injection to  $75.4 \pm 12.8 \text{ HU}$  after injection (Figure 5C). In the meanwhile, we next also conducted T1-weighted MR imaging of mice before and 24 h after i.v. injection of  $\text{WS}_2:\text{Gd}^{3+}$ -PEG nanoflakes ( $2 \text{ mg/mL}, 200 \mu\text{L}$ ). A remarkable brightening effect in the tumors of injected mice was also observed (Figure 5B,C). To understand

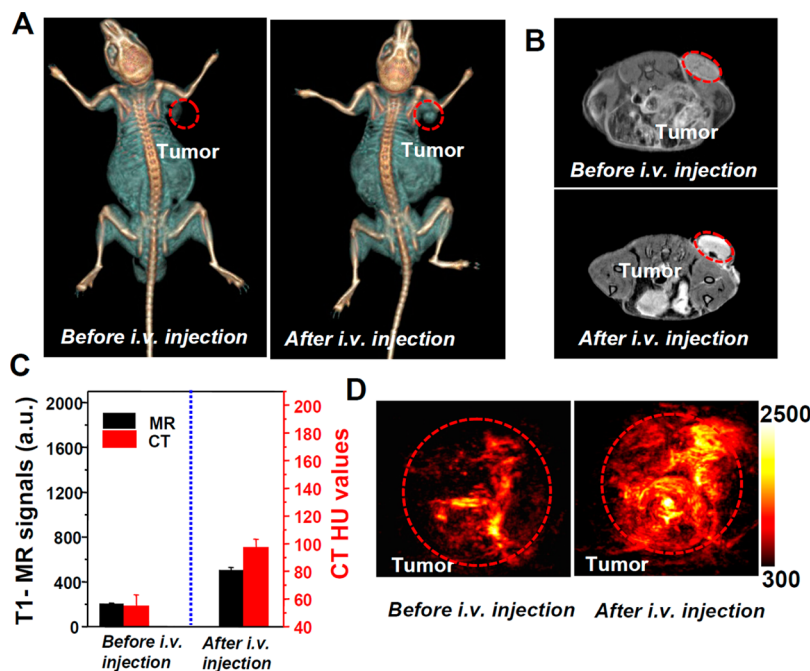


**Figure 5.** *In vivo* triple-model imaging in 4T1-tumor-bearing mice. (A) *In vivo* CT images of mice before and 24 h after i.v. injection with WS<sub>2</sub>:Gd<sup>3+</sup>-3-PEG (5 mg/mL, 200  $\mu$ L). (B) T1-weighted MR images of mice before and 24 h after i.v. injection with WS<sub>2</sub>:Gd<sup>3+</sup>-3-PEG (2 mg/mL, 200  $\mu$ L). (C) Quantified MR and CT signals of tumors from mice before and 24 h after i.v. injection of WS<sub>2</sub>:Gd<sup>3+</sup>-3-PEG based on imaging data in (A) and (B). (D) *In vivo* PA images of tumors on mice before and 24 h after i.v. injection with WS<sub>2</sub>:Gd<sup>3+</sup>-3-PEG (2 mg/mL, 200  $\mu$ L).

the distribution of those nanoagents inside tumors, photoacoustic imaging, with remarkably increased imaging depth and spatial resolution compared to traditional *in vivo* optical imaging,<sup>50–52</sup> was also used in our study to image tumors on mice before and after injection of WS<sub>2</sub>:Gd<sup>3+</sup>-PEG, taking advantages of the strong NIR absorbance of those nanoflakes. While only major blood vasculatures in the untreated tumor could be visualized by PA imaging prior to the injection of WS<sub>2</sub>:Gd<sup>3+</sup>-PEG, strong and evenly distributed photoacoustic signals in the tumor of WS<sub>2</sub>-PEG-injected mice were observed (Figure 5D). The above imaging results collectively confirmed the high passive tumor uptake of WS<sub>2</sub>:Gd<sup>3+</sup>-PEG nanoflakes after systemic administration, likely *via* the enhanced permeability and retention (EPR) effect of cancerous tumors. The exact tumor uptake was measured by ICP to be  $\sim$ 12.7% of injected dose per gram tissue (% ID/g, Supporting Figure S10).

Encouraged by the high tumor accumulation of WS<sub>2</sub>:Gd<sup>3+</sup>-PEG nanoflakes and its strong NIR optical/X-ray absorption, we then carried out *in vivo* combined photothermal/radiation therapy using WS<sub>2</sub>:Gd<sup>3+</sup>-PEG. After being i.v. injected with WS<sub>2</sub>:Gd<sup>3+</sup>-PEG nanoflakes (2 mg/mL, 200  $\mu$ L for each mouse) for 24 h, mice bearing 4T1 tumors were anesthetized and exposed to the 808 nm laser at a power density of 0.5 W/cm<sup>2</sup>. As revealed by infrared (IR) thermal imaging, for mice i.v. injected with WS<sub>2</sub>:Gd<sup>3+</sup>-PEG, their tumors' surface temperature rapidly increased to  $\sim$ 47 °C within 1 min of laser irradiation and remained at this temperature

for 10 min (Figure 6A). In comparison, the tumor temperature on mice without injection under the same irradiation condition showed no significant heating effect.

Next, *in vivo* cancer treatment efficacies of PTT, RT, and combination therapy induced by WS<sub>2</sub>:Gd<sup>3+</sup>-PEG nanoflakes were evaluated. Mice bearing 4T1 tumors (volume  $\sim$ 70 mm<sup>3</sup>) were randomly divided into six groups ( $n = 5$  per group): (i) untreated control, (ii) NIR laser only, (iii) i.v. injection with WS<sub>2</sub>:Gd<sup>3+</sup>-PEG/WS<sub>2</sub>:Gd<sup>3+</sup>-PEG+NIR, (iv) RT only, (v) i.v. injection with WS<sub>2</sub>:Gd<sup>3+</sup>-PEG + RT, (vi) i.v. injection with WS<sub>2</sub>:Gd<sup>3+</sup>-PEG + NIR + RT. The doses of WS<sub>2</sub>:Gd<sup>3+</sup>-PEG nanoflakes were fixed at 20 mg/kg in the above groups. PTT was introduced by 808 nm light irradiation with a power density at 0.5 W/cm<sup>2</sup> for 10 min, while the X-ray radiation dose of RT was 4 Gy. It was found that i.v. injection of WS<sub>2</sub>:Gd<sup>3+</sup>-PEG nanoflakes + NIR laser with mild photothermal heating showed no appreciable effect to the tumor growth (group iii (Figure 6B)). On the other hand, although i.v. injection with WS<sub>2</sub>:Gd<sup>3+</sup>-PEG could enhance the efficacy of RT-induced X-ray treatment (particularly at early days post-treatment), tumors in those groups (groups v and iv) regained the rapid growth speed at later time points. In marked contrast, tumors on mice after WS<sub>2</sub>:Gd<sup>3+</sup>-PEG injection and combined PTT/RT induced by NIR light irradiation first and then X-ray irradiation showed remarkably inhibited tumor growth (group vi), demonstrating the obvious advantage and synergistic effect of combination therapy in comparison to monotherapies.

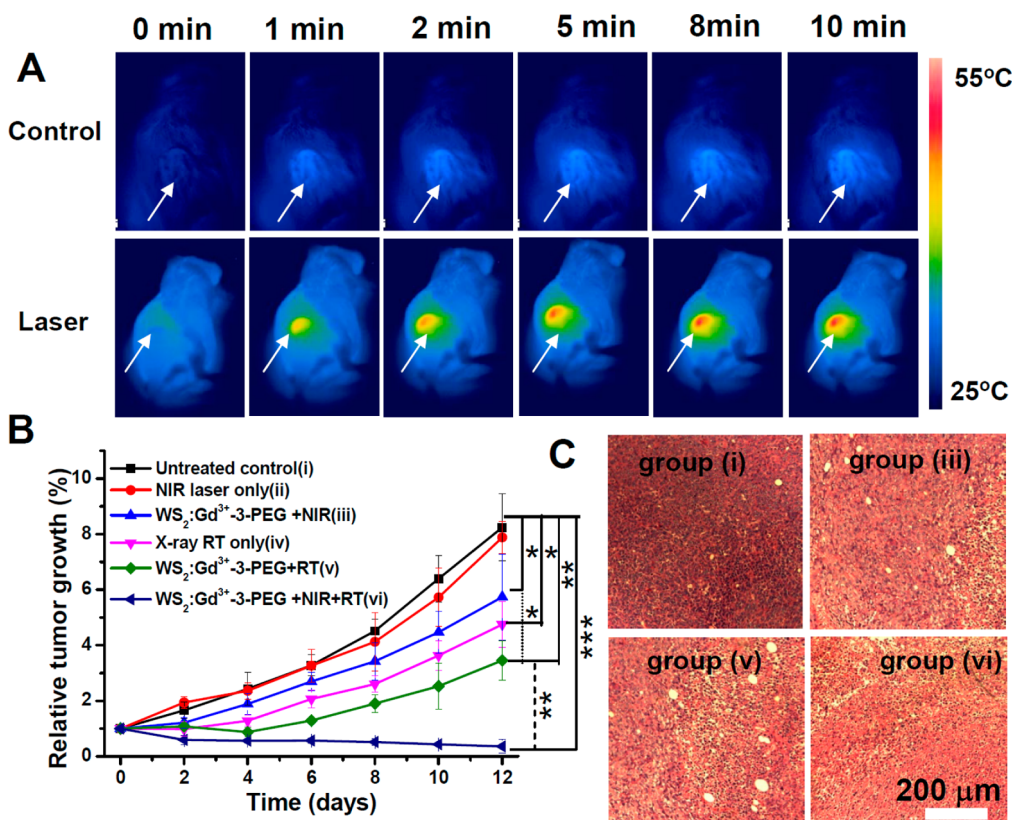


**Figure 6.** *In vivo* combined photothermal and radiation therapy. (A) IR thermal images of 4T1-tumor-bearing mice without (upper row) or with i.v. injection of WS<sub>2</sub>:Gd<sup>3+</sup>-3-PEG (lower row, dose = 20 mg/kg, irradiated at 24 h p.i.), under 808 nm laser irradiation taken at different time intervals. The laser power density was 0.5 W/cm<sup>2</sup>. (B) Tumor volume growth curves of mice after various treatments (5 mice for each group). Group i: untreated control; group ii: NIR laser only; group iii: WS<sub>2</sub>:Gd<sup>3+</sup>-3-PEG + NIR; group iv: X-ray RT alone; group v: WS<sub>2</sub>:Gd<sup>3+</sup>-3-PEG + RT; group vi: WS<sub>2</sub>:Gd<sup>3+</sup>-3-PEG + NIR + RT. PTT was conducted by the 808 nm laser at 0.5 W/cm<sup>2</sup> for 10 min, while the irradiation dose of RT was 4 Gy. Error bars were based on standard error of the mean (SEM). Statistical analysis was performed using the Student's two-tailed *t* test: \**p* < 0.05 and \*\**p* < 0.01. (C) Micrographs of H&E-stained tumor slices in group i, iii, v, and vi, taken 2 days post-treatment.

The antitumor efficacies of different treatments were further assessed by hexatoxylin and eosin (H&E) staining. While tumor cells from WS<sub>2</sub>:Gd<sup>3+</sup>-PEG-nanoflake-injected mice were partially destroyed after irradiating with either an NIR laser (group iii) or X-ray (group v), the combination treatment in group vi could lead to severe destruction of tumor cells, as evidenced by increased vacuoles, condensed nuclei, and changed cell shapes observed from micrographs of H&E-stained tumor slices (Figure 6C). In the meanwhile, no noticeable sign of toxic side effects of the combination therapy with WS<sub>2</sub>:Gd<sup>3+</sup>-PEG was observed in our experiments, as revealed by histological examination of H&E-stained organ slices from WS<sub>2</sub>:Gd<sup>3+</sup>-PEG-injected mice collected 30 days after injection (Supporting Figure S11).

Hypoxia (lack of oxygen), as a common characteristic of the tumor microenvironment, is a negative clinical prognostic factor for a variety of solid tumors due to its critical roles in tumor progression, metastasis, and resistance to mainstream cancer treatment strategies such as RT.<sup>53</sup> The effect of ionizing radiation could be increased under well-oxygenated conditions compared with treatment of hypoxic tumors.<sup>54,55</sup> In order to understand the mechanism of our observed remarkable

synergistic effect in the combined PTT/RT with WS<sub>2</sub>:Gd<sup>3+</sup>-PEG, an immunofluorescence staining assay was carried out by staining blood vessels and hypoxic areas in the tumor with anti-CD31 antibody (red) and anti-pimonidazole antibody (green), respectively (Figure 7), the latter of which was used to stain pimonidazole,<sup>53,56</sup> a hypoxia marker preinjected into tumors before mice were dissected. It was found that the tumor treated with WS<sub>2</sub>:Gd<sup>3+</sup>-PEG + NIR showed an obviously weakened hypoxic area compared to the control group (WS<sub>2</sub>:Gd<sup>3+</sup>-PEG), particularly for cells near blood vessels, indicating that the tumor hypoxia was effectively reduced by mild hyperthermia. Therefore, the overall tumor oxygenation status could be improved immediately after mild PTT, likely owing to the enhanced tumor blood flow under hyperthermia.<sup>52,53</sup> Such a phenomenon may subsequently contribute to the overcoming of hypoxia-associated radio-resistance in the combination therapy.

To our best knowledge, this work is the first report to realize the successful synthesis of TMDC nanostructures evenly doped with different magnetic metal ions via a solution-phase method. Such a method is easy to operate without the need for dangerous chemicals (e.g., *n*-butyllithium to exfoliate bulk TMDCs)<sup>25,57</sup> and

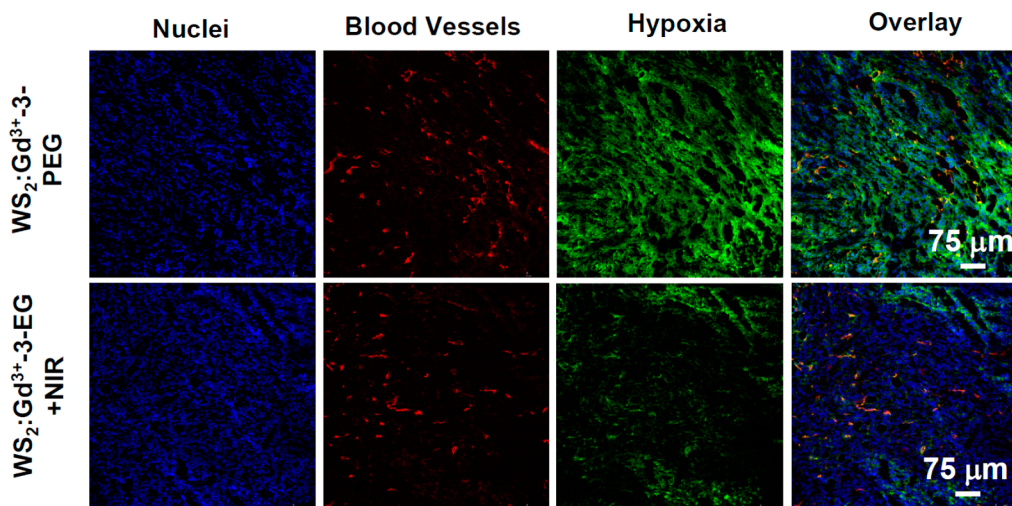


**Figure 7.** Representative immunofluorescence images of tumor slices. The nuclei, blood vessels, and hypoxic areas were stained with DAPI (blue), anti-CD31 antibody (red), and anti-pimonidazole antibody (green), respectively. The mild PTT induced by  $\text{WS}_2:\text{Gd}^{3+}$ -3-PEG resulted in marked reduced hypoxia in the tumor, particularly for tumor cells near blood vessels.

may be extended to other different interesting TMDC materials ( $\text{MoS}_2$ ,  $\text{TiS}_2$ , etc.) or other doping ions. As far as the theranostic application of  $\text{Gd}^{3+}$ -doped  $\text{WS}_2$  nanoflakes is concerned, although the combination of PTT with external RT (triggered by external ionizing irradiation) has been demonstrated in a number of recent studies by intratumoral injection of other nanoagents (local injection has limited clinical relevance),<sup>6,8</sup> our work is the first demonstration of combining these two types of therapeutic approaches to realize synergistic cancer treatment *via* a systemically administrated nanoagent, thanks to the outstanding physical properties (X-ray attenuation, NIR absorbance) of our nanostructure and its effective surface biocompatible modification. Whereas PTT at high temperature heating would induce direct cell necrosis,<sup>58–60</sup> mild PTT as used in this work is able to prompt tumor oxygenation by improving blood flow inside the tumor.<sup>61</sup> Since oxygen-containing radicals are generated in RT under ionizing irradiation, and thus the presence of oxygen would enhance the efficacy of RT,<sup>62,63</sup> the PTT-induced tumor oxygenation is then helpful to circumvent hypoxia-associated tumor radio-resistance.

## CONCLUSION

In summary, a new yet simple method is developed in this work to fabricate various types of metal-ion-doped

$\text{WS}_2$  nanoflakes *via* bottom-up growth. Selecting  $\text{Gd}^{3+}$ -doped  $\text{WS}_2$  with a PEG coating as an example, we have realized imaging-guided combination therapy of cancer. In this nanostructure, the doped  $\text{Gd}^{3+}$  ions offer strong contrast in T1-weighted MR imaging; the strong NIR absorbance of  $\text{WS}_2$ , a typical TMDC structure, enables both PA imaging and PTT therapy; W and Gd elements in the meantime could strongly attenuate X-ray irradiation to allow for CT imaging and enhanced RT treatment. Triple-modal CT/MR/PA imaging uncovered efficient tumor accumulation of these  $\text{WS}_2:\text{Gd}^{3+}$ -PEG nanoflakes after systemic administration into tumor-bearing mice, which were then treated by PTT, RT, or combined PTT/RT. Importantly, owing to the enhanced oxygenation in the tumor after mild PTT, a remarkable synergistic cancer treatment effect was observed in our combined PTT/RT therapy. On one hand, our work presents an interesting type of multifunctional nanoagent promising for cancer theranostics and effective combination therapy to overcome the limitations of conventional radiotherapy. On the other hand, the one-step bottom-up method to synthesize metal-ion-doped  $\text{WS}_2$  nanostructures may be extended to the fabrication of other types of TMDC materials with precisely tunable compositions/properties, for potential applications in catalysis, energy storage, and other areas.

## EXPERIMENTAL SECTION

**Synthesis of  $\text{WS}_2:\text{M}^{n+}$  ( $\text{M} = \text{Fe}^{3+}, \text{Co}^{2+}, \text{Ni}^{2+}, \text{Mn}^{2+}$ , and  $\text{Gd}^{3+}$ ) Nanoflakes.** A typical synthesis procedure is described as follows: 1 mmol of a  $\text{WCl}_6:\text{MCl}_x$  ( $\text{M} = \text{Fe}^{3+}, \text{Co}^{2+}, \text{Ni}^{2+}, \text{Mn}^{2+}$ , and  $\text{Gd}^{3+}$ ) mixture at desired ratios was added into a mixed solvent of 20 mL of oleylamine and 10 mL of 1-octadecene in a three-necked flask (50 mL) at room temperature. The solution was heated to 150 °C to remove water and oxygen under vigorous magnetic stirring in the presence of nitrogen for protection

for ~30 min. Afterward, the temperature of the solution was rapidly raised to 300 °C and kept there for another 30 min in the nitrogen atmosphere. A sulfur solution prepared by dissolving 2 mmol of S powder in 5 mL of OM was then injected into the flask at 300 °C within 10 min. The reaction was kept at 300 °C for 30 min. The ratios of added W:M ( $\text{M} = \text{Fe}^{3+}, \text{Co}^{2+}, \text{Ni}^{2+}, \text{Mn}^{2+}$ , and  $\text{Gd}^{3+}$ ) were chosen as 90:10, 80:20, and 70:30. After the solution was cooled to room temperature,  $\text{WS}_2:\text{Fe}^{3+}$ ,  $\text{WS}_2:\text{Co}^{2+}$ ,  $\text{WS}_2:\text{Ni}^{2+}$ ,  $\text{WS}_2:\text{Mn}^{2+}$ , and  $\text{WS}_2:\text{Gd}^{3+}$  nanoflakes were precipitated by adding anhydrous ethanol (~30 mL),

collected by centrifugation, and washed repetitively with ethanol.

**Surface Modification of WS<sub>2</sub>:Gd<sup>3+</sup> Nanoflakes.** C<sub>18</sub>PMH-PEG was synthesized following a literature procedure.<sup>17</sup> For the PEGylation of nanoflakes, a 2 mL stock solution of WS<sub>2</sub>:Gd<sup>3+</sup> nanoflakes (5 mg/mL) was precipitated by centrifugation. The nanoflakes were washed twice with ethanol and dispersed in chloroform. Another solution of 20 mg of C<sub>18</sub>PMH-PEG polymer in 2 mL of chloroform was then added. The mixture was stirred for 4 h. After blowing-dry chloroform, the residue was readily dissolved in water. The resultant solution was centrifuged at a speed of 3000 rpm to remove large aggregates (with the supernatant collected). Excess PEG molecules were then removed by centrifugation at 14 800 rpm to collect the precipitate, which was then resuspended in water for future use.

**Characterization.** The phase and crystallography of the products were characterized by using a PANalytical X-ray diffractometer equipped with Cu K $\alpha$  radiation ( $\lambda = 0.15406$  nm). A scanning rate of 0.05 deg s<sup>-1</sup> was applied to record the pattern in the 2 $\theta$  range of 10–80°. TEM images of the nanoflakes were obtained using a FEI Tecnai F20 transmission electron microscope equipped with an energy dispersive spectroscope (EDX) at an acceleration voltage of 200 kV. X-ray photoelectron spectra were obtained on an SSI S-Probe XPS spectrometer. FTIR spectra were obtained by a Hyperion (German, Bruker) from 4000 to 400 cm<sup>-1</sup>. Thermogravimetric-differential thermal analysis (TG-DTA) measurements of the products were performed using a Setaram TGA 92 instrument in the temperature range from room temperature to 500 °C at a heating rate of 10 °C/min. UV-vis-NIR spectra were obtained with a PerkinElmer Lambda 750 UV-vis-NIR spectrophotometer. The hydrodynamic diameters of WS<sub>2</sub>:Gd<sup>3+</sup>-PEG nanoflakes were determined by a Zetasizer Nano-ZS (Malvern Instruments, UK). Concentrations of W and Gd were measured by ICP-AES.

**Cell Culture Experiments.** 4T1 murine breast cancer cells were cultured in the standard cell medium recommended by American Type Culture Collection (ATCC), under 37 °C in a 5% CO<sub>2</sub> atmosphere. Cells seeded into 96-well plates at a density of 1 × 10<sup>4</sup> cells per well were incubated with different concentrations of WS<sub>2</sub>:Gd<sup>3+</sup>-PEG nanoflakes for 24 h. Relative cell viabilities were determined by the standard MTT assay. For *in vitro* photothermal therapy, 4T1 cancer cells were incubated with various concentrations of WS<sub>2</sub>:30%Gd<sup>3+</sup>-PEG (WS<sub>2</sub>:Gd<sup>3+</sup>-3-PEG) nanoflakes for 4 h and then irradiated by an 808 nm laser at a power density of 0.8 W/cm<sup>2</sup> for 5 min. The cells were stained with calcine AM/PI for 15 min, washed with PBS, and then imaged by a confocal fluorescence microscope (Leica).

For γ-H2AX immunofluorescence staining, 4T1 cells seeded in 12-well plates at a density of 1 × 10<sup>3</sup> cells per well were incubated with WS<sub>2</sub>:Gd<sup>3+</sup>-3-PEG (0 or 20 μg/mL) for 6 h and then irradiated with X-ray at a dose of 4 Gy. After 2 h of incubation, the cells were fixed by 4% paraformaldehyde for 10 min at room temperature and then rinsed in PBS (pH = 7.4). PBS-incubated cells with and without X-ray irradiation as well as WS<sub>2</sub>:Gd<sup>3+</sup>-3-PEG-treated cells without X-ray exposure were used as controls. The cells were then permeabilized with methanol for 15 min at -20 °C, rinsed with PBS (pH = 7.4), incubated in a blocking buffer (1% BSA in PBS solution) for 1 h at room temperature, and subsequently incubated with primary antibody (mouse monoclonal anti-phosphohistone γ-H2AX, 1:500 in PBS containing 1% BSA) overnight at 4 °C. After PBS washing, the cells were incubated with a fluorescently labeled secondary antibody (sheep anti-mouse Cy633, 1:500 in PBS containing 1% BSA) for 1 h at room temperature. Excess antibody was removed by rinsing the coverslips in PBS. Cell nuclei were stained by DAPI for 5 min at room temperature, before cells were imaged using confocal microscopy (Leica).

For clonogenic assay, 4T1 cells were cultured in six-well plates and incubated at 37 °C for 24 h. Then the cells were treated with culture medium without or with WS<sub>2</sub>:Gd<sup>3+</sup>-3-PEG (0 or 20 μg/mL). After 6 h of incubation, the cells were irradiated by X-ray with different radiation doses (0, 2, 4, and 6 Gy). Afterward the cells were washed with PBS (pH = 7.4) and further incubated in fresh cell culture medium at 37 °C for 10 days, before they were fixed with anhydrous ethanol and stained with crystal

violet (Sigma-Aldrich). The resulting colonies were counted only if they contained more than 50 cells. The surviving fraction = (surviving colonies)/(cells seeded × plating efficiency). The mean surviving fraction was obtained from three parallel tests.

**Tumor Model.** Balb/c mice were obtained from Nanjing Peng Sheng Biological Technology Co. Ltd. and used under protocols approved by Soochow University Laboratory Animal Center. The 4T1 tumors were generated by subcutaneous injection of 1 × 10<sup>6</sup> cells in ~30 μL of serum-free RMPI-1640 medium onto the back of each female Balb/c mice.

**In Vivo Trimodal Imaging.** CT imaging was conducted by using a GE Discovery CT750HD CT instrument. T1-weighted MR images were taken on a 3T clinical MRI scanner (Bruker Biospin Corporation, Billerica, MA, USA) equipped with a small-animal imaging coil. T1-weighted images were acquired using the following parameters: TR 2000 ms; TE 106.4 ms; slice thickness 2.0 mm; slice spacing 0.2 mm; matrix 224 × 192; FOV 10 cm × 10 cm. PA imaging was performed with a preclinical photoacoustic computed tomography scanner (Endra Nexus 128, Ann Arbor, MI, USA). 4T1-tumor-bearing mice were i.v. injected with WS<sub>2</sub>:Gd<sup>3+</sup>-3-PEG (200 μL, 2 mg/mL) for MR and PA imaging. However, due to the lower sensitivity of CT imaging, a higher dose (200 μL, 5 mg/mL) of WS<sub>2</sub>:Gd<sup>3+</sup>-3-PEG was i.v. injected into mice for CT imaging.

**In Vivo RT/PTT Combined Therapy.** Mice bearing 4T1 tumors 24 h post iv injection with WS<sub>2</sub>:Gd<sup>3+</sup>-3-PEG (2 mg/mL, 200 μL, dose = 20 mg/kg) were exposed to the 808 nm NIR laser (Hi-Tech Optoelectronics Co., Ltd. Beijing, China) at a power density of 0.5 W/cm<sup>2</sup> for 10 min for PTT treatment or an X-ray irradiation dose of 4 Gy (3 min) for RT treatment. The tumor surface temperatures were recorded by an IR thermal camera (IRS E50 Pro thermal imaging camera). The tumor sizes were measured by a caliper every other day and calculated as volume = (tumor length) × (tumor width)<sup>2</sup>/2. Relative tumor volumes were calculated as V/V<sub>0</sub> (V<sub>0</sub> is the initial tumor size prior to treatment). Two day after treatment, the tumor tissues in groups 1, 3, 5, and 6 were dissected to make paraffin sections for further H&E staining prepared according to the manufacturer's protocols and observed by a digital microscope (Leica QWin).

**Immunohistochemistry.** Tumor-bearing mice with i.v. injection of WS<sub>2</sub>:Gd<sup>3+</sup>-3-PEG (20 mg/kg) right after NIR laser irradiation (808 nm, 0.5 W/cm<sup>2</sup>, 10 min) were i.v. injected with pimonidazole hydrochloride (60 mg/kg) (Hypoxprobe-1 Plus kit, Hypoxprobe Inc.), which was reductively activated in hypoxic cells and forms stable adducts with thiol (sulfhydryl) groups in proteins, peptides, and amino acids. The tumors were dissected 30 min later and sliced by frozen section. For the detection of pimonidazole, tumor sections were incubated with mouse anti-pimonidazole primary antibody (dilution 1:200, Hypoxprobe Inc.) and then Alex 488-conjugated goat anti-mouse secondary antibody (dilution 1:200, Jackson Inc.) following the vendor's instructions. Staining for blood vessels was performed by incubating tumor sections with rat anti-CD31 mouse monoclonal antibody (dilution 1:200, Biolegend) and rhodamine-conjugated donkey anti-rat secondary antibody (dilution 1:200, Jackson). Cell nuclei were stained with DAPI (dilution 1:5000, Invitrogen). The images were taken with a confocal microscope (Leica SP5).

**Conflict of Interest:** The authors declare no competing financial interest.

**Acknowledgment.** This work was partially supported by the National Natural Science Foundation of China (51302180, 51222203, 51132006), the National "973" Program of China (2012CB932601), and a Project Funded by the Priority Academic Program Development of Jiangsu Higher Education Institutions. L.C. was supported by a Postdoctoral Research Program of Jiangsu Province (1202044C) and a Postdoctoral Science Foundation of China (2013M531400) grant. We thank Prof. Gang Liu at the Center for Molecular Imaging and Translational Medicine at Xiamen University for his great help in photoacoustic imaging.

**Supporting Information Available:** The Supporting Information is available free of charge on the ACS Publications website at DOI: 10.1021/acsnano.5b04606.

Figures S1–S11 (PDF)

## REFERENCES AND NOTES

- Brannon-Peppas, L.; Blanchette, J. O. Nanoparticle and Targeted Systems for Cancer Therapy. *Adv. Drug Delivery Rev.* **2012**, *64*, 206–212.
- Lord, C. J.; Ashworth, A. The DNA Damage Response and Cancer Therapy. *Nature* **2012**, *481*, 287–294.
- Markman, J. L.; Rekechenetskiy, A.; Holler, E.; Ljubimova, J. Y. Nanomedicine Therapeutic Approaches to Overcome Cancer Drug Resistance. *Adv. Drug Delivery Rev.* **2013**, *65*, 1866–1879.
- Jansen, R. L. H.; Beets, G. L. Gastrointestinal Cancer: Which Way is Forward in the Treatment of Rectal Cancer? *Nat. Rev. Clin. Oncol.* **2012**, *10*, 12–13.
- Fan, W.; Shen, B.; Bu, W.; Chen, F.; Zhao, K.; Zhang, S.; Zhou, L.; Peng, W.; Xiao, Q.; Xing, H.; Liu, J.; Ni, D.; He, Q.; Shi, J. Rattle-Structured Multifunctional Nanotheranostics for Synergetic Chemo-/Radiotherapy and Simultaneous Magnetic/Luminescent Dual-Mode Imaging. *J. Am. Chem. Soc.* **2013**, *135*, 6494–6503.
- Xiao, Q.; Zheng, X.; Bu, W.; Ge, W.; Zhang, S.; Chen, F.; Xing, H.; Ren, Q.; Fan, W.; Zhao, K.; Hua, Y.; Shi, J. A Core/Satellite Multifunctional Nanotheranostic for *in Vivo* Imaging and Tumor Eradication by Radiation/Photothermal Synergistic Therapy. *J. Am. Chem. Soc.* **2013**, *135*, 13041–13048.
- Yang, Y.-S.; Carney, R. P.; Stellacci, F.; Irvine, D. J. Enhancing Radiotherapy by Lipid Nanocapsule-Mediated Delivery of Amphiphilic Gold Nanoparticles to Intracellular Membranes. *ACS Nano* **2014**, *8*, 8992–9002.
- Wang, S.; Li, X.; Chen, Y.; Cai, X.; Yao, H.; Gao, W.; Zheng, Y.; An, X.; Shi, J.; Chen, H. A Facile One-Pot Synthesis of a Two-Dimensional MoS<sub>2</sub>/Bi<sub>2</sub>S<sub>3</sub> Composite Theranostic Nanosystem for Multi-Modality Tumor Imaging and Therapy. *Adv. Mater.* **2015**, *27*, 2775–2782.
- Zhou, J.; Liu, Z.; Li, F. Upconversion Nanophosphors for Small-Animal Imaging. *Chem. Soc. Rev.* **2012**, *41*, 1323–1349.
- Huang, X.; El-Sayed, I. H.; Qian, W.; El-Sayed, M. A. Cancer Cell Imaging and Photothermal Therapy in the Near-Infrared Region by Using Gold Nanorods. *J. Am. Chem. Soc.* **2006**, *128*, 2115–2120.
- Cheng, L.; Wang, C.; Feng, L.; Yang, K.; Liu, Z. Functional Nanomaterials for Phototherapies of Cancer. *Chem. Rev.* **2014**, *114*, 10869–10939.
- Robinson, J. T.; Tabakman, S. M.; Liang, Y.; Wang, H.; Sanchez Casalongue, H.; Vinh, D.; Dai, H. Ultrasmall Reduced Graphene Oxide with High Near-Infrared Absorbance for Photothermal Therapy. *J. Am. Chem. Soc.* **2011**, *133*, 6825–6831.
- Tian, Q.; Hu, J.; Zhu, Y.; Zou, R.; Chen, Z.; Yang, S.; Li, R.; Su, Q.; Han, Y.; Liu, X. Sub-10 nm Fe<sub>3</sub>O<sub>4</sub>@Cu<sub>2-x</sub>S Core-Shell Nanoparticles for Dual-Modal Imaging and Photothermal Therapy. *J. Am. Chem. Soc.* **2013**, *135*, 8571–8577.
- Alkilany, A. M.; Thompson, L. B.; Boulos, S. P.; Sisco, P. N.; Murphy, C. J. Gold Nanorods: Their Potential for Photothermal Therapeutics and Drug Delivery, Tempered by The Complexity of Their Biological Interactions. *Adv. Drug Delivery Rev.* **2012**, *64*, 190–199.
- Huang, X.; Tang, S.; Mu, X.; Dai, Y.; Chen, G.; Zhou, Z.; Ruan, F.; Yang, Z.; Zheng, N. Freestanding Palladium Nanosheets with Plasmonic and Catalytic Properties. *Nat. Nanotechnol.* **2011**, *6*, 28–32.
- Liang, X.; Li, Y.; Li, X.; Jing, L.; Deng, Z.; Yue, X.; Li, C.; Dai, Z. PEGLated Poly(pyrrole) Nanoparticles Conjugating Gadolinium Chelates for Dual-Modal MRI/Photoacoustic Imaging Guided Photothermal Therapy of Cancer. *Adv. Funct. Mater.* **2015**, *25*, 1451–1462.
- Cheng, L.; He, W.; Gong, H.; Wang, C.; Chen, Q.; Cheng, Z.; Liu, Z. PEGLated Micelle Nanoparticles Encapsulating a Non-Fluorescent Near-Infrared Organic Dye as a Safe and Highly-Effective Photothermal Agent for *in Vivo* Cancer Therapy. *Adv. Funct. Mater.* **2013**, *23*, 5893–5902.
- Shen, J.; Zhao, L.; Han, G. Lanthanide-doped Upconverting Luminescent Nanoparticle Platforms for Optical Imaging-Guided Drug Delivery and Therapy. *Adv. Drug Delivery Rev.* **2013**, *65*, 744–755.
- Cheng, L.; Yang, K.; Li, Y.; Zeng, X.; Shao, M.; Lee, S.-T.; Liu, Z. Multifunctional Nanoparticles for Upconversion Luminescence/MR Multimodal Imaging and Magnetically Targeted Photothermal Therapy. *Biomaterials* **2012**, *33*, 2215–2222.
- Nguyen, Q. T.; Tsien, R. Y. Fluorescence-Guided Surgery with Live Molecular Navigation: A New Cutting Edge. *Nat. Rev. Cancer* **2013**, *13*, 653–662.
- Coleman, J. N.; Lotya, M.; O'Neill, A.; Bergin, S. D.; King, P. J.; Khan, U.; Young, K.; Gaucher, A.; De, S.; Smith, R. J. Two-Dimensional Nanosheets Produced by Liquid Exfoliation of Layered Materials. *Science* **2011**, *331*, 568–571.
- Voiry, D.; Yamaguchi, H.; Li, J.; Silva, R.; Alves, D. C.; Fujita, T.; Chen, M.; Asefa, T.; Shenoy, V. B.; Eda, G. Enhanced Catalytic Activity in Strained Chemically Exfoliated WS<sub>2</sub> Nanosheets for Hydrogen Evolution. *Nat. Mater.* **2013**, *12*, 850–855.
- Huang, X.; Zeng, Z.; Zhang, H. Metal Dichalcogenide Nanosheets: Preparation, Properties and Applications. *Chem. Soc. Rev.* **2013**, *42*, 1934–1946.
- Zeng, Z.; Yin, Z.; Huang, X.; Li, H.; He, Q.; Lu, G.; Boey, F.; Zhang, H. Single-Layer Semiconducting Nanosheets: High-Yield Preparation and Device Fabrication. *Angew. Chem., Int. Ed.* **2011**, *50*, 11093–11097.
- Chhowalla, M.; Shin, H. S.; Eda, G.; Li, L.-J.; Loh, K. P.; Zhang, H. The Chemistry of Two-Dimensional Layered Transition Metal Dichalcogenide Nanosheets. *Nat. Chem.* **2013**, *5*, 263–275.
- Feng, J.; Sun, X.; Wu, C.; Peng, L.; Lin, C.; Hu, S.; Yang, J.; Xie, Y. Metallic Few-Layered VS<sub>2</sub> Ultrathin Nanosheets: High Two-Dimensional Conductivity for In-Plane Supercapacitors. *J. Am. Chem. Soc.* **2011**, *133*, 17832–17838.
- Lukowski, M. A.; Daniel, A. S.; Meng, F.; Forticaux, A.; Li, L.; Jin, S. Enhanced Hydrogen Evolution Catalysis from Chemically Exfoliated Metallic MoS<sub>2</sub> Nanosheets. *J. Am. Chem. Soc.* **2013**, *135*, 10274–10277.
- Chou, S. S.; Kaehr, B.; Kim, J.; Foley, B. M.; De, M.; Hopkins, P. E.; Huang, J.; Brinker, C. J.; David, V. P. Chemically Exfoliated MoS<sub>2</sub> as Near-Infrared Photothermal Agents. *Angew. Chem.* **2013**, *125*, 4254–4258.
- Zhu, C.; Zeng, Z.; Li, H.; Li, F.; Fan, C.; Zhang, H. Single-Layer MoS<sub>2</sub>-Based Nanoprobes for Homogeneous Detection of Biomolecules. *J. Am. Chem. Soc.* **2013**, *135*, 5998–6001.
- Cheng, L.; Liu, J.; Gu, X.; Gong, H.; Shi, X.; Liu, T.; Wang, C.; Wang, X.; Liu, G.; Xing, H. PEGLated WS<sub>2</sub> Nanosheets as A Multifunctional Theranostic Agent for *in Vivo* Dual-Modal CT/Photoacoustic Imaging Guided Photothermal Therapy. *Adv. Mater.* **2014**, *26*, 1886–1893.
- Yin, W.; Yan, L.; Yu, J.; Tian, G.; Zhou, L.; Zheng, X.; Zhang, X.; Yong, Y.; Li, J.; Gu, Z. High-Throughput Synthesis of Single-Layer MoS<sub>2</sub> Nanosheets as a Near-Infrared Photothermal-Triggered Drug Delivery for Effective Cancer Therapy. *ACS Nano* **2014**, *8*, 6922–6933.
- Qian, X.; Shen, S.; Liu, T.; Cheng, L.; Liu, Z. Two-Dimensional TiS<sub>2</sub> Nanosheets for *in Vivo* Photoacoustic Imaging and Photothermal Cancer Therapy. *Nanoscale* **2015**, *7*, 6380–6387.
- Liu, J.; Zheng, X.; Yan, L.; Zhou, L.; Tian, G.; Yin, W.; Wang, L.; Liu, Y.; Hu, Z.; Gu, Z.; Chen, C.; Zhao, Y. Bismuth Sulfide Nanorods as a Precision Nanomedicine for *in Vivo* Multi-modal Imaging-Guided Photothermal Therapy of Tumor. *ACS Nano* **2015**, *9*, 696–707.
- Li, J.; Jiang, F.; Yang, B.; Song, X.-R.; Liu, Y.; Yang, H.-H.; Cao, D.-R.; Shi, W.-R.; Chen, G.-N. Topological Insulator Bismuth Selenide as a Theranostic Platform for Simultaneous Cancer Imaging and Therapy. *Sci. Rep.* **2013**, *3*, 1987–7.
- Liu, T.; Wang, C.; Gu, X.; Gong, H.; Cheng, L.; Shi, X.; Feng, L.; Sun, B.; Liu, Z. Drug Delivery with PEGLated MoS<sub>2</sub> Nanosheets for Combined Photothermal and Chemotherapy of Cancer. *Adv. Mater.* **2014**, *26*, 3433–3440.
- Ma, M.; Huang, Y.; Chen, H.; Jia, X.; Wang, S.; Wang, Z.; Shi, J. Bi<sub>2</sub>S<sub>3</sub>-Embedded Mesoporous Silica Nanoparticles for Efficient Drug Delivery and Interstitial Radiotherapy Sensitization. *Biomaterials* **2015**, *37*, 447–455.

37. Liu, T.; Shi, S.; Liang, C.; Shen, S.; Cheng, L.; Wang, C.; Song, X.; Goel, S.; Barnhart, T. E.; Cai, W. Iron Oxide Decorated MoS<sub>2</sub> Nanosheets with Double PEGylation for Chelator-free Radiolabeling and Multimodal Imaging Guided Photothermal Therapy. *ACS Nano* **2015**, *9*, 950–960.
38. Yang, G.; Gong, H.; Liu, T.; Sun, X.; Cheng, L.; Liu, Z. Two-Dimensional Magnetic WS<sub>2</sub>@Fe<sub>3</sub>O<sub>4</sub> Nanocomposite with Mesoporous Silica Coating for Drug Delivery and Imaging-Guided Therapy of Cancer. *Biomaterials* **2015**, *60*, 62–71.
39. Cheng, L.; Huang, W.; Gong, Q.; Liu, C.; Liu, Z.; Li, Y.; Dai, H. Ultrathin WS<sub>2</sub> Nanoflakes as a High-Performance Electrocatalyst for the Hydrogen Evolution Reaction. *Angew. Chem., Int. Ed.* **2014**, *53*, 7860–7863.
40. Gong, Q.; Cheng, L.; Liu, C.; Zhang, M.; Feng, Q.; Ye, H.; Zeng, M.; Xie, L.; Liu, Z.; Li, Y. Ultrathin MoS<sub>2</sub>(1-x)Se<sub>2</sub>x Alloy Nanoflakes for Electrocatalytic Hydrogen Evolution Reaction. *ACS Catal.* **2015**, *5*, 2213–2219.
41. Liu, Y.; Ai, K.; Liu, J.; Yuan, Q.; He, Y.; Lu, L. A High-Performance Ytterbium-Based Nanoparticulate Contrast Agent for *In Vivo* X-Ray Computed Tomography Imaging. *Angew. Chem., Int. Ed.* **2012**, *51*, 1437–1442.
42. Liu, Y.; Ai, K.; Lu, L. Nanoparticulate X-ray Computed Tomography Contrast Agents: From Design Validation to *In Vivo* Applications. *Acc. Chem. Res.* **2012**, *45*, 1817–1827.
43. Xing, H.; Zheng, X.; Ren, Q.; Bu, W.; Ge, W.; Xiao, Q.; Zhang, S.; Wei, C.; Qu, H.; Wang, Z. Computed Tomography Imaging-Guided Radiotherapy by Targeting Upconversion Nanocubes with Significant Imaging and Radiosensitization Enhancements. *Sci. Rep.* **2013**, *3*, 1751–9.
44. Xia, A.; Chen, M.; Gao, Y.; Wu, D.; Feng, W.; Li, F. Gd<sup>3+</sup> Complex-Modified NaLuF<sub>4</sub>-Based Upconversion Nanophosphors for Trimodality Imaging of NIR-to-NIR Upconversion Luminescence, X-Ray Computed Tomography and Magnetic Resonance. *Biomaterials* **2012**, *33*, 5394–5405.
45. Rieter, W. J.; Kim, J. S.; Taylor, K. M. L.; An, H.; Lin, W.; Tarrant, T.; Lin, W. Hybrid Silica Nanoparticles for Multimodal Imaging. *Angew. Chem., Int. Ed.* **2007**, *46*, 3680–3682.
46. Bridot, J.-L.; Faure, A.-C.; Laurent, S.; Rivière, C.; Billotey, C.; Hiba, B.; Janier, M.; Josserand, V.; Coll, J.-L.; Vander Elst, L.; Muller, R.; Roux, S.; Perriat, P.; Tillement, O. Hybrid Gadolinium Oxide Nanoparticles: Multimodal Contrast Agents for *In Vivo* Imaging. *J. Am. Chem. Soc.* **2007**, *129*, 5076–5084.
47. Bryant, L. H.; Brechbiel, M. W.; Wu, C.; Bulte, J. W. M.; Herynek, V.; Frank, J. A. Synthesis and Relaxometry of High-Generation (G = 5, 7, 9, and 10) PAMAM Dendrimer-DOTA-Gadolinium Chelates. *J. Mammary Gland Biol. Neoplasia* **1999**, *9*, 348–352.
48. Gong, H.; Dong, Z.; Liu, Y.; Yin, S.; Cheng, L.; Xi, W.; Xiang, J.; Liu, K.; Li, Y.; Liu, Z. Engineering of Multifunctional Nano-Micelles for Combined Photothermal and Photodynamic Therapy under the Guidance of Multimodal Imaging. *Adv. Funct. Mater.* **2014**, *24*, 6492–6502.
49. Kinner, A.; Wu, W.; Staudt, C.; Iliakis, G. γ-H2AX in Recognition and Signaling of DNA Double-Strand Breaks in the Context of Chromatin. *Nucleic Acids Res.* **2008**, *36*, 5678–5694.
50. Moon, G. D.; Choi, S.-W.; Cai, X.; Li, W.; Cho, E. C.; Jeong, U.; Wang, L. V.; Xia, Y. A New Theranostic System based on Gold Nanocages and Phase-Change Materials with Unique Features for Photoacoustic Imaging and Controlled Release. *J. Am. Chem. Soc.* **2011**, *133*, 4762–4765.
51. Cobley, C. M.; Chen, J.; Cho, E. C.; Wang, L. V.; Xia, Y. Gold Nanostructures: A Class of Multifunctional Materials for Biomedical Applications. *Chem. Soc. Rev.* **2011**, *40*, 44–56.
52. Huang, P.; Lin, J.; Li, W.; Rong, P.; Wang, Z.; Wang, S.; Wang, X.; Sun, X.; Aronova, M.; Niu, G. Biodegradable Gold Nanovesicles with an Ultrastrong Plasmonic Coupling Effect for Photoacoustic Imaging and Photothermal Therapy. *Angew. Chem.* **2013**, *125*, 14208–14214.
53. Gordijo, C. R.; Abbasi, A. Z.; Amini, M. A.; Lip, H. Y.; Maeda, A.; Cai, P.; O'Brien, P. J.; DaCosta, R. S.; Rauth, A. M.; Wu, X. Y. Design of Hybrid MnO<sub>2</sub>-Polymer-Lipid Nanoparticles with Tunable Oxygen Generation Rates and Tumor Accumulation for Cancer Treatment. *Adv. Funct. Mater.* **2015**, *25*, 1858–1872.
54. Fan, W.; Bu, W.; Shen, B.; He, Q.; Cui, Z.; Liu, Y.; Zheng, X.; Zhao, K.; Shi, J. Intelligent MnO<sub>2</sub> Nanosheets Anchored with Upconversion Nanoprobes for Concurrent pH/H<sub>2</sub>O<sub>2</sub>-Responsive UCL Imaging and Oxygen-Elevated Synergetic Therapy. *Adv. Mater.* **2015**, *27*, 4155–4161.
55. Horsman, M. R.; Overgaard, J. Hyperthermia: A Potent Enhancer of Radiotherapy. *Clin. Oncol.* **2007**, *19*, 418–426.
56. Thambi, T.; Deepagan, V.; Yoon, H. Y.; Han, H. S.; Kim, S.-H.; Son, S.; Jo, D.-G.; Ahn, C.-H.; Suh, Y. D.; Kim, K. Hypoxia-Responsive Polymeric Nanoparticles for Tumor-Targeted Drug Delivery. *Biomaterials* **2014**, *35*, 1735–1743.
57. Wang, Q. H.; Kalantar-Zadeh, K.; Kis, A.; Coleman, J. N.; Strano, M. S. Electronics and Optoelectronics of Two-Dimensional Transition Metal Dichalcogenides. *Nat. Nanotechnol.* **2012**, *7*, 699–712.
58. Melamed, J. R.; Edelstein, R. S.; Day, E. S. Elucidating The Fundamental Mechanisms of Cell Death Triggered by Photothermal Therapy. *ACS Nano* **2015**, *9*, 6–11.
59. Zhou, Z.; Kong, B.; Yu, C.; Shi, X.; Wang, M.; Liu, W.; Sun, Y.; Zhang, Y.; Yang, H.; Yang, S. Tungsten Oxide Nanorods: An Efficient Nanoplatform for Tumor CT Imaging and Photothermal Therapy. *Sci. Rep.* **2014**, *4*, 3653.
60. Pérez-Hernández, M.; del Pino, P.; Mitchell, S. G.; Moros, M.; Stepien, G.; Pelaz, B.; Parak, W. J.; Gálvez, E. M.; Pardo, J.; de la Fuente, J. M. Dissecting the Molecular Mechanism of Apoptosis during Photothermal Therapy Using Gold Nanoprism. *ACS Nano* **2015**, *9*, 52–61.
61. Sun, X.; Li, X.-F.; Russell, J.; Xing, L.; Urano, M.; Li, G. C.; Humm, J. L.; Ling, C. C. Changes in Tumor Hypoxia Induced by Mild Temperature Hyperthermia as Assessed by Dual-tracer Immunohistochemistry. *Radiat. Oncol.* **2008**, *88*, 269–276.
62. Song, C.; Park, H.; Lee, C.; Griffin, R. Implications of Increased Tumor Blood Flow and Oxygenation Caused by Mild Temperature Hyperthermia in Tumor Treatment. *Int. J. Hyperthermia* **2005**, *21*, 761–767.
63. Song, C.; Shakil, A.; Osborn, J.; Iwata, K. Tumour Oxygenation is Increased by Hyperthermia at Mild Temperatures. *Int. J. Hyperthermia* **2009**, *25*, 91–95.